applied sciences

MDPI

Article

Spatial Prediction of Daily Maximum Equivalent Ice Thickness on Transmission Lines Based on Multi-Source Data Fusion

Yu Wu [1,*], Xianglun Nie [1], Jia Luo [2], Baolong Xie [2], Guiheng Liu [2] and Chao Yuan [2]

[1] Bijie Power Supply Bureau of Guizhou Power Grid Co., Ltd., Bijie 551700, China; 19923625408@163.com
[2] College of Electrical and Information Engineering, Hunan University, Changsha 410082, China; xiebaolong1206@163.com (J.L.); x142144@hnu.edu.cn (B.X.); guihengliu@hnu.edu.cn (G.L.); yc2300@hnu.edu.cn (C.Y.)
* Correspondence: jia_luo@hnu.edu.cn

Abstract

Accurate estimation of transmission-line icing is important for regional power-grid risk assessment, particularly in mountainous areas characterized by complex terrain and strong spatial variability. This study develops a multi-source data fusion framework for spatial prediction of daily maximum equivalent ice thickness on transmission lines in Guizhou Province, China. Meteorological variables, topographic factors, remote-sensing information, and geographic coordinates were integrated with operational ice-thickness observations from 160 monitoring stations. Three tree-based ensemble models, namely Random Forest, XGBoost, and LightGBM, were evaluated using a station-based spatial hold-out strategy in which all observations from the test stations were completely excluded from model development. LightGBM achieved the highest R^2 (0.8131) and the lowest RMSE (2.5162 mm), whereas XGBoost achieved the lowest MAE (1.0244 mm), indicating comparable spatial generalization performance between the two gradient-boosting models. Stratified error analysis showed that prediction errors increased substantially for extreme icing observations above the 90th percentile, and all three models exhibited negative mean bias errors in this range, indicating systematic underestimation of severe icing. Gain-based feature importance and SHAP analysis showed that temperature-related variables, geographic location, and elevation provided the main predictive information for the fitted model, while their contributions should not be interpreted as direct evidence of physical causality. The optimized LightGBM model was further applied to 1 km gridded environmental predictors to generate a spatially continuous daily icing map, demonstrating pronounced spatial heterogeneity across Guizhou. These results indicate that the proposed framework can support regional-scale estimation of daily maximum equivalent ice thickness at previously unseen monitoring locations, while further improvement is required for extreme icing prediction and transfer to other regions or time periods.

Keywords: ice thickness prediction; transmission lines; multi-source data fusion; machine learning

Check for updates

Academic Editor: Mauro Lo Brutto

Received: 5 August 2026
Revised: 13 September 2026
Accepted: 23 September 2026
Published: 27 October 2026

Copyright: © 2026 by the authors. Licensee MDPI, Basel, Switzerland. This article is an open access article distributed under the terms and conditions of the Creative Commons Attribution (CC BY) license.

1. Introduction

Icing on overhead transmission lines represents one of the most severe meteorological hazards affecting the safety and reliability of power systems. The accumulation of ice on conductors can significantly increase mechanical loading, induce conductor galloping, cause tower deformation and insulation failures, and ultimately result in large-scale power outages [1,2]. Severe icing events frequently occur in mountainous and humid regions, where

complex terrain and variable atmospheric conditions lead to strong spatial heterogeneity in icing processes [3,4]. The formation of transmission-line icing is governed by coupled thermodynamic, aerodynamic, and microphysical processes involving air temperature, liquid water content, precipitation, humidity, and wind conditions, making accurate regional-scale icing assessment highly challenging [5]. In China, the 2008 southern China ice storm caused extensive damage to transmission infrastructure and highlighted the vulnerability of power systems to extreme icing conditions [6,7]. With the continuous expansion of transmission networks into complex mountainous areas, reliable regional icing monitoring and prediction have become increasingly important for power-grid operation, maintenance, and disaster prevention [5,7].

Existing transmission-line icing prediction approaches can generally be categorized into physics-based models, empirical-statistical methods, and numerical weather prediction (NWP)-based approaches. Physics-based models describe ice accretion mechanisms according to heat transfer, mass transfer, aerodynamic effects, and conductor characteristics, providing important physical insights into icing formation processes [8,9]. However, their application over large spatial domains is often limited by the requirement for detailed meteorological and microphysical parameters, which are difficult to obtain continuously at high spatial resolution [10]. Empirical models establish statistical relationships between icing thickness and environmental variables based on historical observations [11]. Although these methods are computationally efficient, their performance strongly depends on the representativeness of monitoring stations and may degrade under complex terrain and heterogeneous climatic conditions. Recently, NWP models combined with data assimilation techniques have been applied for regional icing prediction by providing spatially continuous atmospheric information [12,13]. Nevertheless, uncertainties associated with atmospheric model resolution, parameterization schemes, and local terrain representation remain major limitations, particularly in mountainous regions [14]. Therefore, accurately estimating regional-scale icing thickness still requires approaches capable of integrating multi-source environmental information and capturing nonlinear relationships between icing processes and their controlling factors [15].

Machine learning (ML) methods have recently attracted increasing attention in icing prediction because of their ability to model complex nonlinear relationships between icing observations and heterogeneous environmental variables. Compared with traditional statistical approaches, ML algorithms can simultaneously utilize multiple predictors and automatically extract interactions among meteorological, topographic, and environmental factors [16,17]. Various ML models, including artificial neural networks, support vector machines, random forests, and ensemble learning algorithms, have been successfully applied to icing-related prediction problems. For transmission-line icing thickness estimation, AdaBoost combined with least-squares weighted support vector machines (LS-WSVM) has been developed to establish nonlinear relationships between icing thickness and influencing factors [18]. Deep learning approaches, such as convolutional neural networks (CNNs), have also been explored for extracting complex patterns from multidimensional icing-related observations and achieved promising prediction accuracy [19]. Furthermore, optimization-based machine learning models, such as KPCA-GWO-SVM, have been proposed to improve convergence performance and prediction accuracy for icing thickness estimation [20]. Beyond single-station prediction, recent studies have demonstrated the potential of integrating remote sensing data and ensemble learning methods for spatial environmental modeling, providing new opportunities for large-scale icing field reconstruction [21–23].

Despite these advances, several limitations remain in current ML-based transmission-line icing studies. First, most existing studies mainly focus on short-term forecasting or single-site prediction, while regional-scale spatial mapping of icing thickness over complex

terrain remains insufficiently investigated [24,25]. Second, conventional random sample division strategies may introduce spatial information leakage when measurements from the same monitoring locations are distributed into both training and testing datasets, resulting in overestimated model performance [26]. Third, high-resolution spatial icing products generated by integrating operational monitoring observations with multi-source environmental variables are still limited, especially in mountainous regions with strong spatial variability. Therefore, developing a robust framework that combines ground-based icing measurements, meteorological information, topographic characteristics, and remote sensing indicators is essential for improving regional icing assessment. In this study, a multi-source data fusion framework based on machine learning is developed for estimating transmission-line icing thickness in Guizhou Province. By integrating real icing observations from power-grid monitoring stations with meteorological, terrain, and remote sensing features, the proposed framework aims to achieve accurate and spatially continuous icing thickness prediction. Furthermore, the trained model is extended from station-level estimation to 1 km gridded daily maximum equivalent icing thickness mapping, providing a practical approach for regional icing risk assessment and intelligent power-grid operation in complex mountainous environments.

2. Study Area and Data

2.1. Study Area

This study focuses on Guizhou Province, located in the eastern part of the Yunnan-Guizhou Plateau in southwestern China (Figure 1). The province is characterized by its vast highland terrain, with an average elevation of approximately 1100 m above sea level. The landscape is famously described as "eight parts mountains, one part water, and one part farmland," with mountains and hills accounting for about 92.5% of its total area. This pronounced topography forces prevailing moist air masses to ascend, a key mechanism for cloud and precipitation formation. Furthermore, Guizhou is a global epicenter of karst landform development. The complex micro-terrain features, such as peaks, depressions, and valleys, created by widespread karst processes lead to highly localized microclimates. This results in significant spatial variability in meteorological conditions over short distances, making icing events extremely heterogeneous band challenging to predict uniformly.

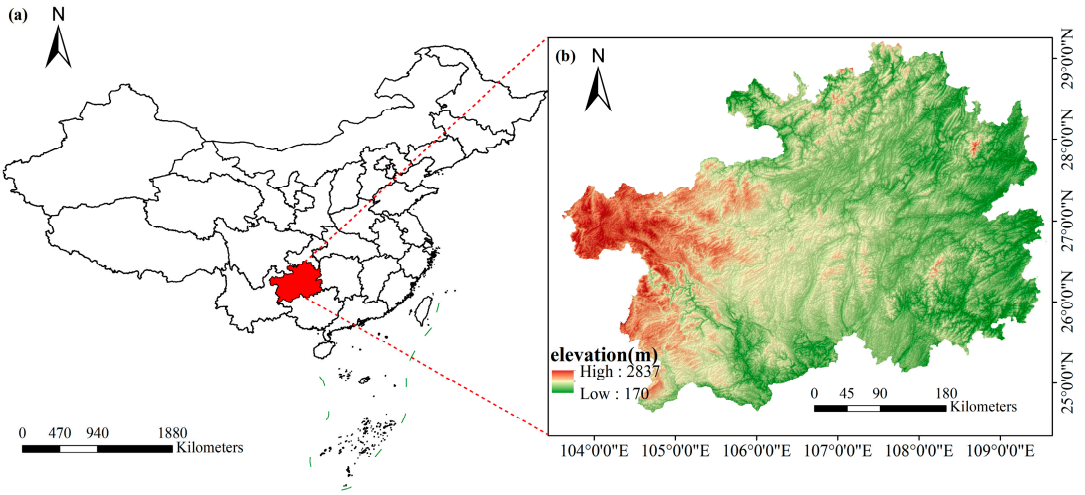


Figure 1. Geographical location and topography of the study area: (**a**) location of Guizhou Province in China; (**b**) elevation distribution of Guizhou Province.

Guizhou experiences a humid subtropical monsoon climate. While winters are not severely cold in terms of absolute temperature, they are marked by persistent damp, cloudy,

and sunless conditions. The region is highly prone to a specific and destructive winter weather phenomenon known as "ning dong" or freezing rain. When this kind of "freezing rain" collides with structures such as power lines, poles or branches at or below zero degrees Celsius, it will immediately freeze. This process may lead to rapid and large ice accumulation, posing a serious threat to infrastructure.

2.2. Label Data

Due to the topographic characteristics of Guizhou Province, manual ice observation has a limited scope and cannot cover high-altitude or remote areas. To ensure that icing data encompass as much of Guizhou's diverse terrain as possible and to achieve a more uniform spatial distribution—thereby enhancing the robustness and generalization ability of the training model—icing thickness data were obtained from sensors installed on transmission lines by China Southern Power Grid and processed through terminal systems [27]. The data represent the nominal equivalent ice thickness, which standardizes conductors of different heights and diameters to a conductor at a height of 10 m above ground with a diameter of 26.8 mm. It also converts ice of varying densities and shapes into a uniform annular ice coating around the conductor with a density of 0.9 g/cm^3, where the ice thickness refers to the radial thickness of the annulus. Through this standardization process, ice thickness data are rendered comparable across different regions and operating conditions, allowing for meaningful statistical analysis and comparison of icing on transmission lines. Because the objective of this work is to investigate regional spatial prediction based on standardized operational monitoring data, the sensing hardware itself is not treated as a modeling variable or evaluated comparatively in this study.

With the upgrading of power grid equipment in recent years, monitoring terminals from earlier years may produce data with significant errors owing to outdated devices. Therefore, we selected monitoring terminal data from 2019 onward as the labeled ice thickness dataset. This dataset comprises a total of 160 monitoring terminals, whose distribution is shown in Figure 2. The dataset covers five winter seasons from 2019/2020 to 2023/2024, and only observations from December, January, and February were included. The original monitoring records were available at a nominal temporal interval of 10 min. After quality control, the observations were aggregated separately by monitoring station and calendar day. A station-day observation was retained only when at least 12 valid intraday records were available. For each retained station-day, the maximum valid equivalent ice-thickness measurement was extracted as the response variable. Accordingly, the modeled quantity represents the daily maximum equivalent ice thickness observed at an individual monitoring location rather than a province-wide maximum or a statistically derived design ice load.

2.3. Feature Data

2.3.1. Meteorological Data

The meteorological data adopted were from ChinaMet: A High-resolution Multi-element Meteorological Driving Dataset for China via Multi-source Data Fusion. The dataset is provided by National Cryosphere Desert Data Center (https://www.ncdc.ac.cn, accessed on 20 December 2025). This dataset integrates multi-source remote sensing data, reanalysis data, and observational data from over 2000 meteorological stations in China. It was developed using a knowledge-guided Machine Learning (ML) approach combined with climate-field-assisted spatial downscaling techniques. The multi-source remote sensing data include remote sensing precipitation products, such as the multi-satellite integrated retrieval GPM precipitation dataset (https://disc.gsfc.nasa.gov/, accessed on 20 December 2025) and global daily precipitation products based on ASCAT satellite soil moisture data, a gridded

daily NDVI dataset derived from NOAA AVHRR surface reflectance products (https://www.ncei.noaa.gov/, accessed on 22 December 2025), and a land surface temperature dataset collected and processed by MODIS (https://ladsweb.modaps.eosdis.nasa.gov/, accessed on 16 December 2025). The reanalysis data used are the latest ERA5-Land product released by the European Centre for Medium-Range Weather Forecasts (ECMWF) (https://cds.climate.copernicus.eu/, accessed on 20 December 2025).

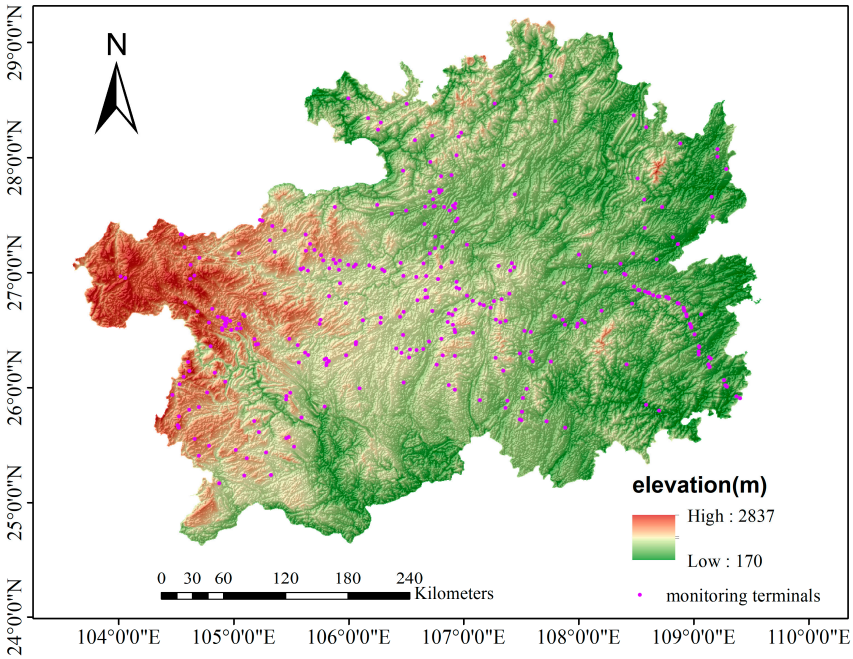


Figure 2. Distribution of monitoring terminals.

The dataset comprises eight meteorological elements: precipitation, mean 2-m air temperature near the surface, maximum temperature, minimum temperature, 10-m wind speed, relative humidity, surface pressure, and potential evapotranspiration. Six meteorological variables were selected as predictors in the present study: precipitation (pre), mean 2-m air temperature (tmpmean), maximum temperature (tmpmax), minimum temperature (tmpmin), 10-m wind speed (wind), and relative humidity (rhu). The selection was primarily guided by their physical relevance to atmospheric icing and their consistent availability within the selected ChinaMet dataset during the study period, rather than by a data-driven feature-screening procedure. Temperature variables characterize the thermal conditions controlling whether atmospheric water can freeze on the conductor, while relative humidity and precipitation provide information on moisture availability. Wind speed is related to the transport and impaction of water droplets onto exposed structures. These variables therefore represent the principal thermal, moisture, and aerodynamic conditions associated with atmospheric icing and are consistent with the physical and empirical factors discussed in previous transmission-line icing studies. Surface pressure and potential evapotranspiration, although available in the original ChinaMet product, were not retained because the present study prioritized variables with more direct relevance to short-term icing formation and accumulation.

The dataset covers the period from 1980 to 2024 with a daily temporal resolution and spatial resolution of 0.1° and 0.01°. To align temporally with the terminal monitoring data and to enable more accurate ice thickness prediction, the subset from 2019 to 2024 was selected, with a spatial resolution of 0.01° (approximately 1 km).

It should be noted that several variables with direct physical relevance to icing, including precipitation phase, liquid water content, droplet-size characteristics, and wind direction, were not included in the current model because they are not provided by the selected ChinaMet product with the same spatial and temporal coverage as the predictors used in this study. Their omission may limit the representation of detailed microphysical processes, particularly during severe icing events.

2.3.2. Topographic Data

For topographic data, the NASA SRTM Digital Elevation dataset was utilized. This dataset originates from an international research initiative that acquired near-global-scale digital elevation models. The SRTM V3 product (SRTM Plus), provided by NASA JPL at a resolution of 1 arc-second (approximately 30 m), was directly downloaded via Google Earth Engine for the required temporal and spatial extents. The downloaded data represent elevation. To enrich the topographic characterization, slope and aspect were further derived from the elevation data.

$$slope = arctan\left(\sqrt{\left(\frac{\partial z}{\partial x}\right)^2 + \left(\frac{\partial z}{\partial y}\right)^2}\right) \times \frac{180}{\pi} \quad (1)$$

$$aspect = a\ tan2\left(-\frac{\partial z}{\partial y}, \frac{\partial z}{\partial x}\right) \times \frac{180}{\pi} \quad (2)$$

In Equations (1) and (2), x and y denote the coordinate values in the horizontal and vertical directions (i.e., east–west and north–south directions), respectively, while z represents the elevation or altitude value. After processing, both slope and aspect are expressed in degrees (°). The slope angle ranges from 0° to 90°; the aspect angle, after conversion using Equation (3), results in a range of 0° to 360°.

$$aspect_{adjust} = \begin{cases} aspect + 360^{\circ} & aspect < 0 \\ aspect & \text{otherwise} \end{cases} \quad (3)$$

2.3.3. NDVI Data

The land cover beneath transmission lines, which are erected across diverse locations, is complex and varied. Different surface features typically influence local climatic conditions such as humidity and air pressure, thereby directly or indirectly affecting ice accretion thickness. Therefore, this study incorporates the Normalized Difference Vegetation Index (NDVI) to characterize the impact of different land cover types. The NDVI data from the Landsat Collection 2 Tier 1 Level 2 Annual NDVI Composite, provided by the U.S. Geological Survey (USGS), were utilized. This dataset, accessible directly via the Google Earth Engine platform, has a spatial resolution of 30 m.

2.4. Data Fusion and Dataset Creation

The original 10-min monitoring records were first sorted by terminal ID and timestamp, and duplicate records associated with the same terminal and timestamp were removed while retaining the last valid observation. Records containing negative ice-thickness values or other values identified as invalid during the original data-quality screening were treated as missing. Negative air-temperature values were retained because they are physically meaningful, whereas physically invalid negative values of precipitation, wind speed, and relative humidity were excluded. After quality control, the records were aggregated separately by monitoring station and calendar day. Station-days with fewer than 12 valid ice-thickness observations were excluded, and the maximum valid intraday measurement was retained as the daily maximum equivalent ice thickness.

To construct the training sample set required for the machine learning model, this study precisely aligned and matched multi-source heterogeneous feature data with the ice-thickness label data across both temporal and spatial dimensions (Figure 3). The core principle was to extract and associate all feature variables from the same spatiotemporal point for each "station-time" observation, i.e., one label data point.

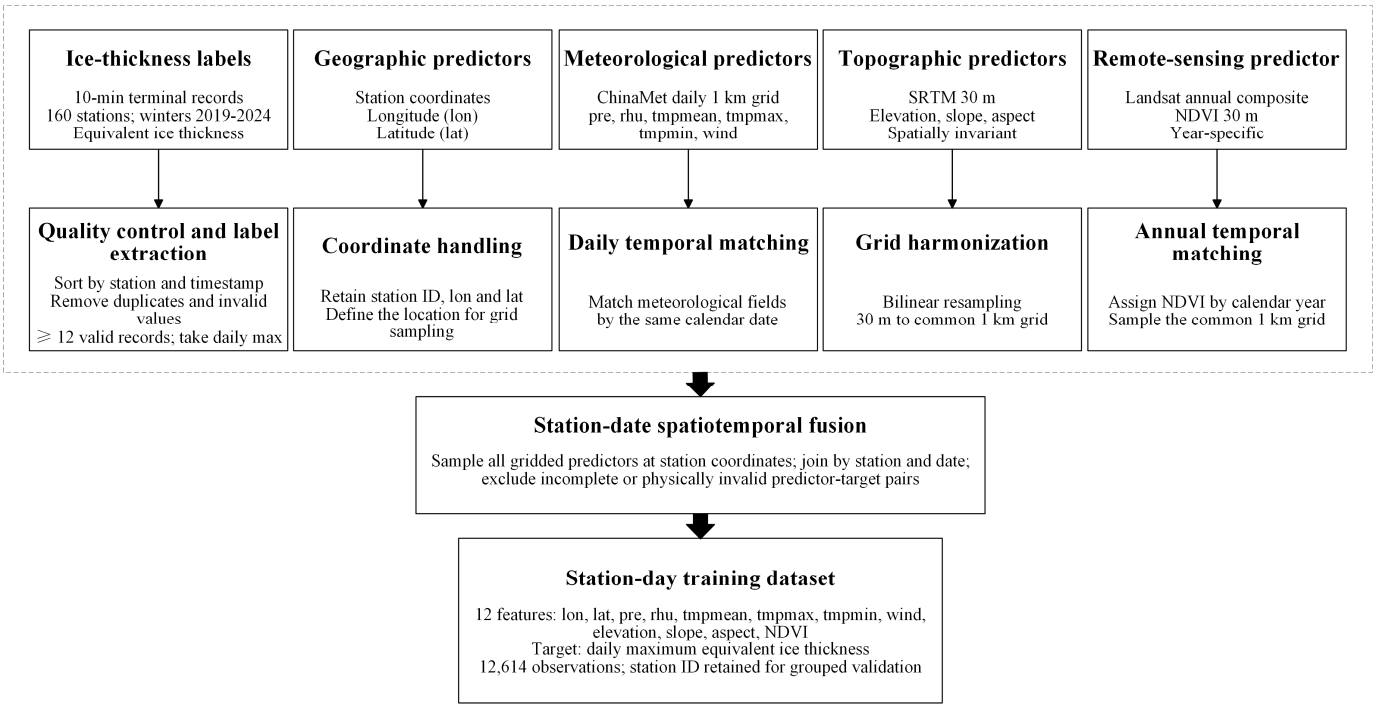


Figure 3. Workflow of multi-source data fusion and station-day dataset construction for icing thickness prediction.

Temporal matching was performed according to the temporal characteristics of each data source. The ice-thickness target represents the daily maximum value for each monitoring station. Daily meteorological predictors were therefore matched directly to the ice-thickness target using the same calendar date. Topographic variables, including elevation, slope, and aspect, were treated as temporally invariant during the study period. NDVI was represented by an annual composite; consequently, all station-day observations within the same calendar year were assigned the corresponding annual NDVI field. This matching strategy produced one unified feature vector for each valid station-day observation.

Spatially, the meteorological, topographic, and NDVI raster datasets were transformed to a common 1 km grid using bilinear interpolation. The unified grid was then used as the spatial reference for both station-level feature extraction and subsequent regional prediction. For each monitoring station, predictor values were sampled from the corresponding 1 km gridded fields according to the station coordinates. Bilinear interpolation was adopted because the predictors considered here are continuous environmental variables, allowing values at locations between neighboring grid-cell centers to be estimated smoothly without introducing an additional geostatistical model.

The original SRTM-derived topographic variables and Landsat NDVI data have a native spatial resolution of approximately 30 m, whereas the selected meteorological data have a resolution of approximately 1 km. To construct a spatially consistent predictor set, the finer-resolution datasets were resampled to the common 1 km grid. This harmonization enables direct integration of the multi-source predictors but inevitably smooths part of the sub-grid topographic and land-surface variability.

After spatial and temporal alignment, station-day observations containing unresolved missing values in the predictor variables were excluded. Only observations with a complete and physically valid predictor–target combination were retained for subsequent model development. The final dataset consisted of 12,614 station-day observations collected from 160 monitoring stations. Because multiple daily observations were available for each monitoring station, these observations were not regarded as spatially independent samples during model validation. Monitoring-station identity was therefore retained as a grouping variable during dataset partitioning and cross-validation to prevent observations from the same location from appearing in both the training and test sets.

3. Methodology

3.1. Machine Learning Models

The relationship between the ice thickness to be estimated in this study and various features exhibits strong nonlinearity, making it unsuitable for traditional shallow models like linear regression. Furthermore, the training dataset comprises 12,614 samples, which is a medium-sized dataset. Employing deep learning models based on gradient descent, such as neural networks, would be highly prone to overfitting. Consequently, this study opts for tree-based ensemble models, selecting Random Forest (RF), XGBoost and LightGBM for training and testing [28]. This category of models can automatically handle nonlinear relationships and feature interactions, making them particularly well-suited for processing this type of tabular data.

Random Forest is a classic Bagging ensemble algorithm. It constructs multiple decision trees through bootstrap sampling and aggregates their results via a voting (for classification) or averaging (for regression) mechanism, significantly reducing the variance inherent in a single tree. Its core randomness is manifested in two aspects: firstly, row sampling of the training data, and secondly, at each node split within a tree, selecting the optimal split feature from only a random subset of all features. This "double randomness" ensures diversity among the trees, enhancing the model's overall robustness and generalization ability. For regression tasks, its prediction formula is:

$$\hat{y}_{RF} = \frac{1}{B}\sum_{b=1}^{B} T_b(x) \tag{4}$$

In Equation (4), x is the input feature vector, T_b represents the b-th tree, and B is the total number of trees. Random Forest is relatively insensitive to hyperparameters, less prone to overfitting, and often serves as a stable baseline model.

XGBoost builds decision trees in a sequential manner, where each new tree aims to correct the residuals of the previous ensemble of trees. It expands the objective function using a second-order Taylor expansion and incorporates a regularization term to control model complexity:

$$\mathcal{L}^{(t)} = \sum_{i=1}^{N} l\left(y_i, \hat{y}_i^{(t-1)} + f_t(x_i)\right) + \Omega(f_t) \tag{5}$$

In Equation (5), $\mathcal{L}$ is the loss function, $\hat{y}_i^{(t-1)}$ is the prediction from the first $t-1$ trees, f_t is the t-th tree, and Ω is the regularization term. XGBoost efficiently finds the optimal split points through an exact approximate algorithm and supports optimizations like sparsity-aware splitting and weighted quantile sketch, giving it outstanding performance in both accuracy and computational efficiency. It can finely capture the complex mapping relationships between features and the target through continuous optimization of the loss function.

LightGBM introduces Gradient-based One-Side Sampling (GOSS) and Exclusive Feature Bundling (EFB) [29]. Unlike traditional level-wise tree growth, it focuses on samples

that are more challenging for the current predictions, greatly accelerating training speed without significant loss of accuracy. Its tree structure grows leaf-wise, which can more effectively reduce loss for the same number of splits compared to level-wise growth.

3.2. Evaluation Metrics

This study employs several commonly used evaluation metrics to assess model predictive performance. The coefficient of determination (R^2) measures the proportion of variance in the target variable explained by the model and serves as the core metric for evaluating prediction accuracy in this work. The root-mean-square error (RMSE), which shares the same unit as the target variable, reflects the average deviation between predicted and actual values, facilitating practical interpretation. The mean absolute error (MAE) is less sensitive to outliers, providing a robust estimate of prediction error. In addition, mean bias error (MBE) was used to quantify systematic prediction bias. MBE was calculated as the mean difference between predicted and observed ice thickness. A positive MBE indicates an overall tendency toward overestimation, whereas a negative MBE indicates underestimation. Values closer to zero indicate a smaller systematic bias. These metrics are used to evaluate the models in this study, and their calculation formulas are as follows:

$$R^2 = 1 - \frac{\sum_{i=1}^{N} (y_i - \hat{y}_i)^2}{\sum_{i=1}^{N} (y_i - \overline{y})^2} \tag{6}$$

$$\mathrm{RMSE} = \sqrt{\frac{1}{N}\sum_{i=1}^{n} (y_i - \hat{y}_i)^2} \tag{7}$$

$$MAE = \frac{1}{N}\sum_{i=1}^{N} |y_i - \hat{y}_i| \tag{8}$$

$$MBE = \frac{1}{N}\sum_{i=1}^{N} (\hat{y}_i - y_i) \tag{9}$$

where y_i is the observed value, $\hat{y}_i$ is the predicted value, $\overline{y}$ is the mean of the observed values, and N is the number of samples.

To further assess model performance across different icing intensities, the independent test observations were stratified according to the distribution of observed ice thickness. Observations at or below the 50th percentile (P_{50} = 3.41 mm) were classified as low-icing cases, observations between the 50th and 90th percentiles (3.41 < y ≤ 11.976 mm) as moderate-icing cases, and observations above the 90th percentile (P_{90} = 11.976 mm) as extreme-icing cases. The three subsets contained 1265, 1005, and 253 observations, respectively. RMSE, MAE, and MBE were calculated separately for each icing-intensity level. This stratified evaluation was used only for performance diagnosis and did not participate in model training or hyperparameter optimization.

3.3. Experimental Design

The primary objective of this study is to estimate the spatial distribution of daily maximum equivalent ice thickness at a 1 km resolution by integrating meteorological, topographic, remote-sensing, and geographic predictors. After spatiotemporal matching of all predictor variables and labels, the predictors were standardized to have a mean of 0 and a standard deviation of 1 as part of a unified preprocessing procedure. It should be noted that RF, XGBoost, and LightGBM are tree-based models and are generally insensitive to monotonic feature scaling; therefore, the standardization step was not expected to improve model accuracy or convergence. It was retained only to maintain a consistent preprocessing

format across the multi-source predictor variables. Subsequently, the machine learning models were constructed. During the training phase, a search space for key hyperparameters was designed for each model, and the Bayesian optimization algorithm was employed for hyperparameter tuning.

To avoid potential information leakage caused by repeated observations from the same monitoring station and to provide a more rigorous assessment of spatial generalization, the dataset was partitioned at the monitoring-station level rather than at the individual-observation level. Approximately 20% of the 160 monitoring stations, corresponding to 2523 station-day observations, were reserved as an independent spatial test set. All observations associated with these test stations were completely excluded from model training and hyperparameter optimization. The remaining monitoring stations, comprising 10,091 station-day observations, were used for model development and grouped five-fold cross-validation. During Bayesian hyperparameter optimization, five-fold grouped cross-validation was performed using monitoring-station identity as the grouping variable, ensuring that all observations from the same station were assigned to the same fold. Consequently, none of the monitoring locations included in the independent test set were encountered during either model training or validation. This strategy provides a more stringent assessment of spatial generalization to previously unseen monitoring locations within the study region.

All models were trained using Mean Squared Error (MSE) as the loss function for the regression task, ultimately producing estimates of the daily maximum ice thickness at corresponding locations based on the input features. The overall workflow, illustrated in Figure 4, can be divided into three key steps:

The first step involves data fusion, quality control, and feature preprocessing. This study selected 12 feature variables at the sample point locations: geographic information includes longitude (lon) and latitude (lat); meteorological information includes precipitation (prec), relative humidity (rhu), mean near-surface 2-m air temperature (tmpmean), maximum temperature (tmpmax), minimum temperature (tmpmin), and near-surface 10-m wind speed (wind); remote sensing data includes the Normalized Difference Vegetation Index (NDVI); topographic information includes elevation, slope, and aspect. For consistency in the preprocessing pipeline, all predictor variables were standardized before model input. Because the three models are tree-based ensemble methods, this scaling operation does not alter the ordering of feature values and was not introduced to improve model convergence or predictive performance. The target variable is the daily maximum ice thickness at the sample point, obtained from sensors after terminal processing. The study filtered all daily data, removing outliers such as negative ice thickness values caused by sensor malfunctions or other factors.

The second step focuses on model training and hyperparameter optimization under a station-grouped validation framework. Bayesian optimization was combined with grouped five-fold cross-validation, in which monitoring-station identity was used as the grouping variable. All observations from the same monitoring station were kept within the same fold throughout the optimization procedure. Bayesian optimization models the relationship between hyperparameters and model performance using a probabilistic model, guiding the next search step with an acquisition function, enabling it to find a near-optimal hyperparameter combination with minimal iterations. For models with high-dimensional hyperparameter spaces like XGBoost and LightGBM, Bayesian optimization can efficiently search through the space by leveraging surrogate models to compress spatial information. It performs fine-grained searches in promising regions while also exploring areas of high uncertainty, making it more likely to find a global optimum. A grouped five-fold cross-validation strategy was applied to the model-development set. The monitoring stations, rather than

individual station-day observations, were divided into five mutually exclusive groups. In each iteration, all observations from one group of stations were used for validation, while observations from the remaining four groups were used for training. Each monitoring station therefore appeared in only one fold, eliminating overlap of station-specific observations between the training and validation subsets. The mean validation performance across the five folds was used as the objective for Bayesian hyperparameter optimization.

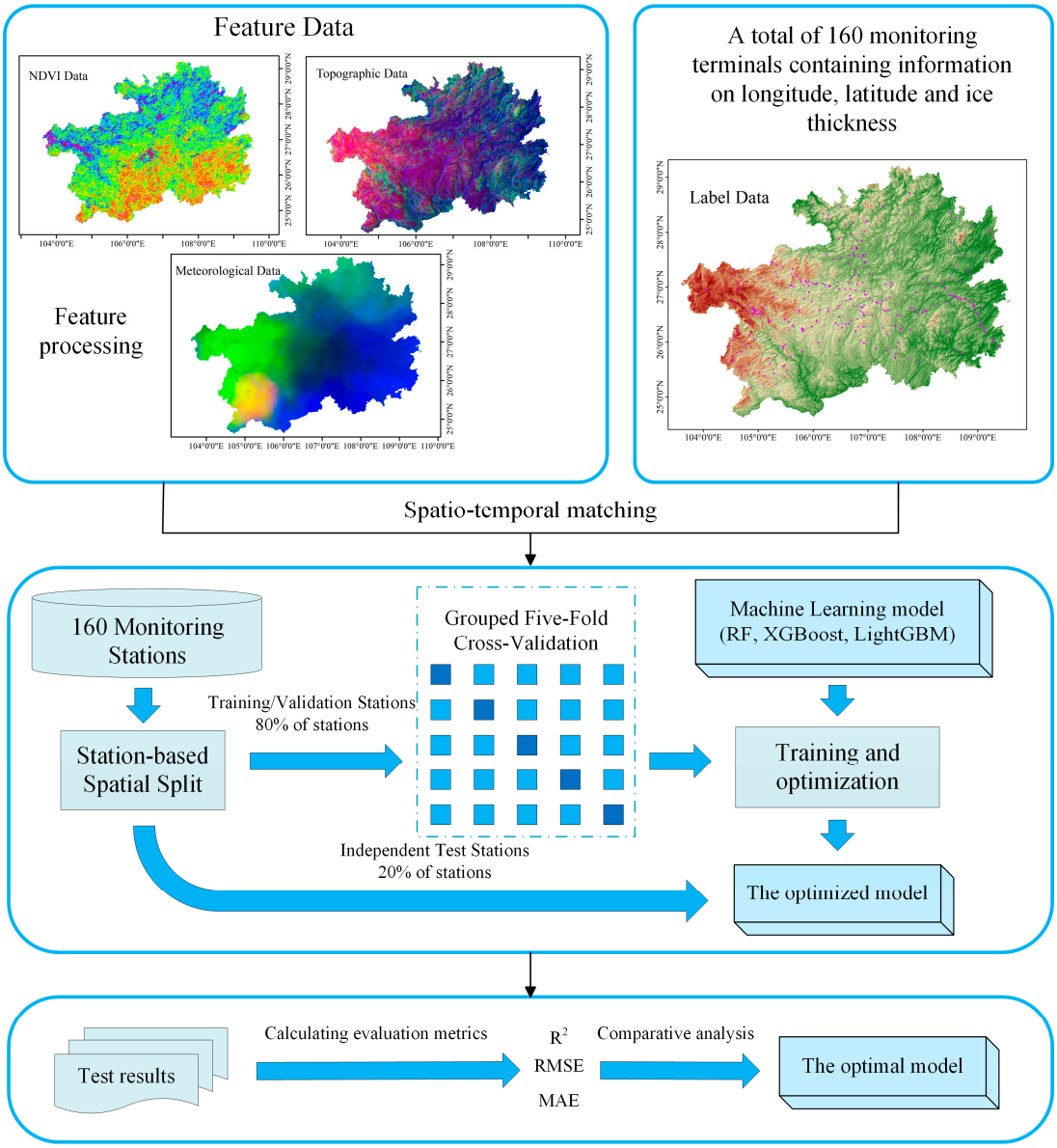


Figure 4. A diagram of the overall framework of this study.

After training and optimization, the optimal hyperparameter combinations for each model are as follows: RF: 'bootstrap': False, 'max_depth': 26, 'max_features': 1, 'min_impurity_decrease': 0.0, 'min_samples_leaf': 1, 'min_samples_split': 2, 'n_estimators': 50. XGBoost: 'max_depth': 12, 'learning_rate': 0.3, 'min_child_weight': 1.011, 'subsample': 0.5, 'colsample_bytree': 1, 'gamma': 0, 'reg_alpha': 9.4299, 'reg_lambda': 2.88. LightGBM: 'num_leaves': 79, 'max_depth': 12, 'learning_rate': 0.068, 'feature_fraction': 0.757, 'bagging_fraction': 0.796, 'bagging_freq': 5, 'lambda_l1': 0.464444, 'lambda_l2': 6.075, 'min_data_in_leaf': 12, 'verbose': −1.

The final step is model evaluation and comparative analysis. The trained machine learning models are evaluated on the held-out test set, and their performance metrics are calculated. The primary objective is to identify the optimal model for predicting the daily maximum ice thickness distribution using the available feature data through comparative analysis. In addition, an NDVI ablation experiment was performed using the same station-based spatial validation strategy to evaluate the contribution of the remote-sensing vegetation predictor to the final LightGBM model.

4. Results and Discussion

4.1. Data Exploration and Feature Relationships

Figure 5 presents scatter plots of selected predictor variables against the observed ice thickness. The three temperature variables show broadly similar inverse patterns, with larger ice-thickness observations occurring mainly under relatively low-temperature conditions, whereas high ice thickness is rarely observed at higher temperatures. Relative humidity shows a generally positive association with ice thickness, although substantial dispersion is present across the observed range. Elevation exhibits a similar increase in the upper range of observed ice thickness at higher values, but the wide scatter indicates that elevation alone does not determine icing severity. The relationships between ice thickness and precipitation, wind speed, NDVI, and slope are less distinct in the individual scatter plots and appear to be nonlinear or strongly dispersed. These exploratory patterns are used only to describe pairwise associations and should not be interpreted as independent causal effects because icing is influenced by multiple correlated environmental factors.

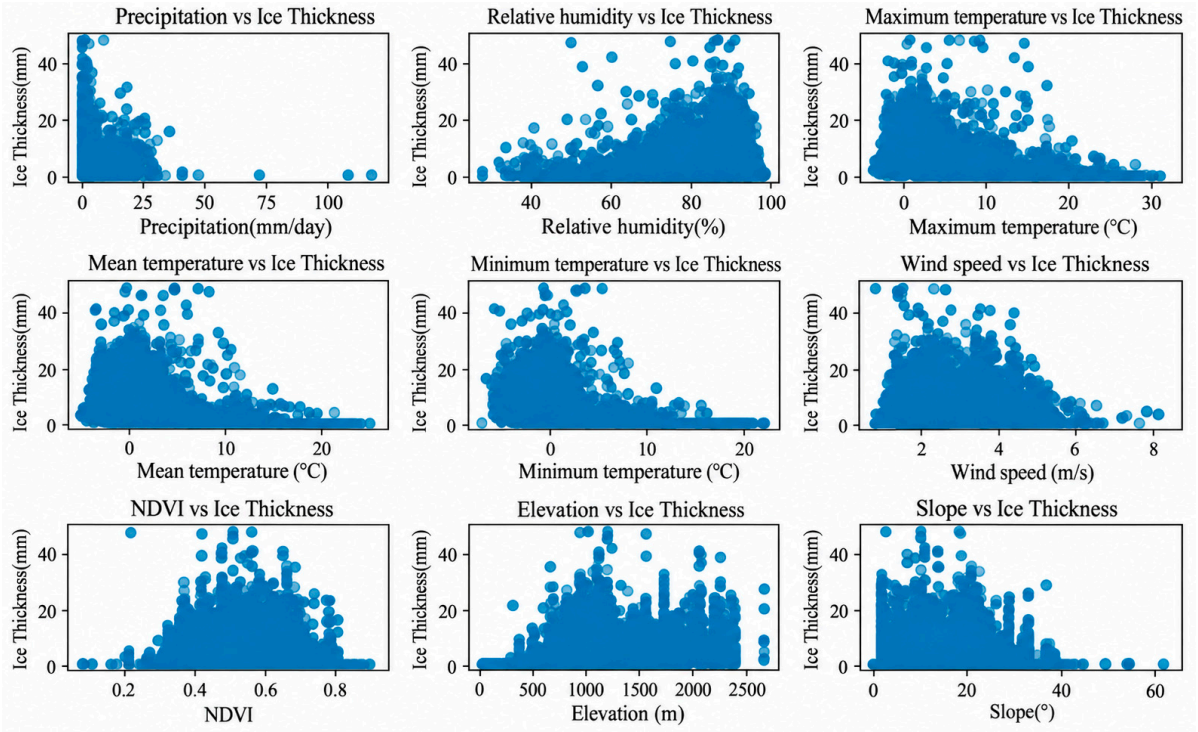


Figure 5. Scatter plots of selected predictor variables against observed ice thickness.

The Pearson correlation coefficient heatmap (Figure 6) quantifies the linear relationships observed in the scatterplots. Consistent with physical expectations, ice thickness shows a positive correlation with elevation and relative humidity, and a strong negative correlation with all temperature variables. It is noteworthy that a significant negative correlation exists between elevation and mean temperature, confirming the well-known effect

of the environmental temperature lapse rate. Although tree-based ensemble methods are less sensitive to multicollinearity than conventional linear regression models in terms of predictive performance, strong dependence among correlated predictors can still affect the allocation and interpretation of feature importance. This issue is therefore considered explicitly in the subsequent SHAP-based interpretation. The direct correlation between NDVI and ice thickness is relatively low, suggesting its role may be more contextual or interactive rather than directly causal, a nuance potentially better captured by the nonlinear models.

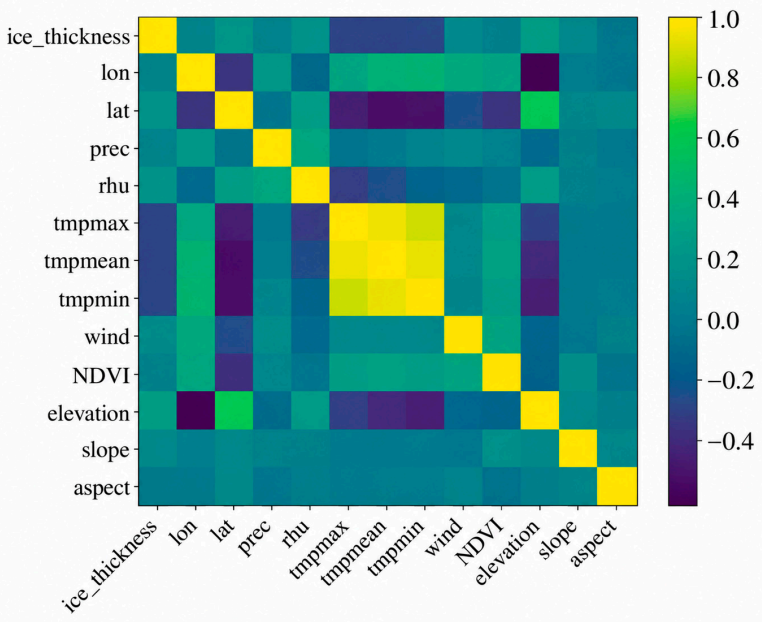


Figure 6. Pearson correlation coefficient heat map.

4.2. Model Performance and Error Analysis

4.2.1. Overall Model Performance

The three machine learning models were evaluated using the independent test stations under the station-based spatial hold-out validation scheme, and the results are presented in Table 1. Compared with an observation-level random split, this evaluation is more stringent because none of the monitoring locations in the test set were included during model training or hyperparameter optimization. RF achieved an R^2 of 0.7501, an RMSE of 2.9093 mm, and an MAE of 1.5352 mm. XGBoost substantially improved the predictive performance, yielding an R^2 of 0.8104, an RMSE of 2.5341 mm, and the lowest MAE of 1.0244 mm. LightGBM achieved the highest R^2 of 0.8131 and the lowest RMSE of 2.5162 mm, with an MAE of 1.0928 mm. The overall MBE values were 0.1957 mm for RF, 0.0299 mm for XGBoost, and 0.0564 mm for LightGBM, indicating relatively small net bias across the complete independent test set. However, the near-zero overall MBE masks substantial bias variation across icing-intensity levels.

Table 1. Performance comparison of three ML models on the test set.

ML Model	R^2	RMSE (mm)	MAE (mm)	MBE (mm)
RF	0.7501	2.9093	1.5352	0.1957
XGBoost	0.8104	2.5341	**1.0244**	**0.0299**
LightGBM	**0.8131**	**2.5162**	1.0928	0.0564

Note: Bold values indicate the best performance for each metric among the three models; for MBE, the value closest to zero is considered the best.

The performance difference between XGBoost and LightGBM was relatively small. LightGBM showed a slight advantage in terms of explained variance and RMSE, whereas XGBoost achieved a lower MAE and MBE. Overall, both gradient-boosting models maintained good predictive performance when applied to spatially independent monitoring locations that were completely unseen during model development. Based on its slightly higher R^2 and lower RMSE, LightGBM was retained for subsequent model interpretation and spatial prediction. However, the close performance of XGBoost indicates that the superiority of LightGBM is modest rather than absolute.

To examine whether the predictive performance was primarily driven by geographic coordinates, an additional ablation experiment was conducted by removing longitude and latitude from the LightGBM input features while retaining the same station-based spatial validation strategy. As shown in Table 2, removing the geographic coordinates reduced R^2 from 0.8131 to 0.7949, while RMSE increased from 2.5162 to 2.6355 mm and MAE increased from 1.0928 to 1.3654 mm. Nevertheless, the model retained substantial predictive capability in the absence of longitude and latitude. These results indicate that geographic coordinates provide useful information on broad regional spatial variability that is not fully represented by the available environmental predictors, but they are not the sole source of predictive skill. More importantly, because the test stations were completely excluded from model development, the geographic coordinates of the test locations were also unseen during training, substantially reducing the risk that the model performance resulted from memorization of station-specific locations.

Table 2. Effect of geographic-coordinate predictors on LightGBM performance under station-based spatial hold-out validation.

Input Features	R^2	RMSE (mm)	MAE (mm)
With longitude and latitude	**0.8131**	**2.5162**	**1.0928**
Without longitude and latitude	0.7949	2.6355	1.3654

Note: Bold values indicate the better performance between the two model configurations.

Figure 7 compares the monitored and predicted ice thickness values obtained from the three models at the independent test stations. RF exhibits greater dispersion around the 1:1 reference line, particularly at higher observed ice thicknesses. In comparison, both XGBoost and LightGBM produce predictions that are more concentrated around the reference line. The overall scatter patterns of XGBoost and LightGBM are similar, consistent with their close R^2 and RMSE values in Table 1. However, visual agreement with the 1:1 line alone is insufficient to assess systematic bias or performance for extreme icing observations.

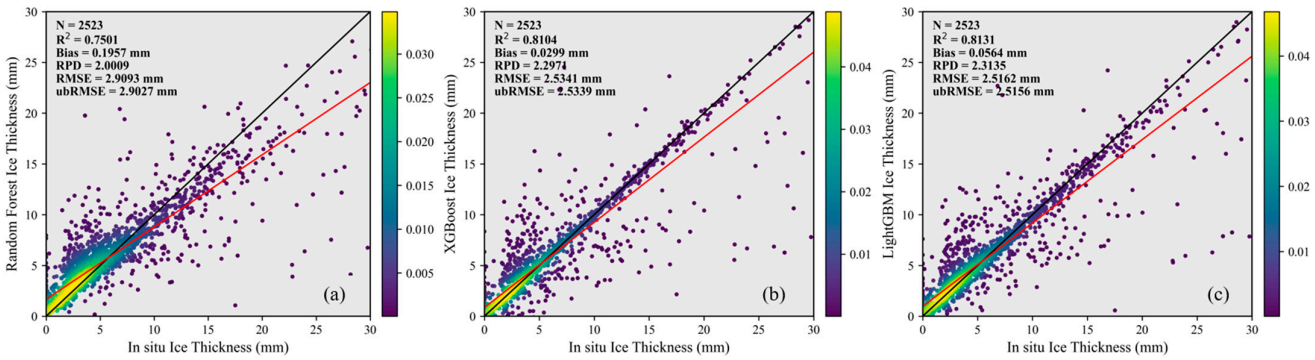


Figure 7. Comparison between monitored and predicted ice thickness values for (**a**) RF, (**b**) XGBoost, and (**c**) LightGBM under station-based spatial hold-out validation. The black line represents the 1:1 reference line, and the red line represents the fitted regression line.

4.2.2. Performance Across Icing-Intensity Levels and Residual Analysis

To examine whether the overall evaluation metrics adequately represent model behavior across different icing intensities, the independent test observations were further divided into low-, moderate-, and extreme-icing subsets according to the 50th and 90th percentiles of observed ice thickness. As shown in Table 3, prediction errors increased substantially with icing intensity for all three models. For low-icing conditions, XGBoost achieved the lowest RMSE and MAE of 1.3280 mm and 0.6345 mm, respectively, followed closely by LightGBM. Under moderate icing conditions, LightGBM yielded the lowest RMSE of 2.3643 mm, while XGBoost produced the lowest MAE of 1.0558 mm. The largest errors occurred in the extreme-icing subset, confirming that high ice-thickness observations are substantially more difficult to predict than low and moderate cases.

Table 3. Prediction errors of the three machine learning models under different icing-intensity levels.

Model	Icing Level	RMSE (mm)	MAE (mm)	MBE (mm)
RF	Low	1.6796	0.9911	0.9313
RF	Moderate	2.5574	1.4674	0.3654
RF	Extreme	6.6571	4.5244	−4.1569
XGBoost	Low	**1.3280**	**0.6345**	**0.4212**
XGBoost	Moderate	2.4167	**1.0558**	**0.1775**
XGBoost	Extreme	5.6588	**2.8499**	**−2.5134**
LightGBM	Low	1.3489	0.6979	0.4913
LightGBM	Moderate	**2.3643**	1.0947	0.2090
LightGBM	Extreme	**5.6422**	3.0602	−2.7239

Note: Bold values indicate the best performance within each icing-intensity level; lower RMSE and MAE values indicate better performance, while for MBE, the value closest to zero is considered the best.

For extreme icing observations above 11.976 mm, RF exhibited the largest errors, with an RMSE of 6.6571 mm, an MAE of 4.5244 mm, and an MBE of −4.1569 mm. Both gradient-boosting models substantially reduced the upper-tail prediction error. LightGBM achieved the lowest extreme-case RMSE of 5.6422 mm, whereas XGBoost achieved the lowest MAE of 2.8499 mm and the smallest absolute bias, with an MBE of −2.5134 mm. Compared with RF, the extreme-case RMSE was reduced by approximately 15% for both XGBoost and LightGBM, while the MAE decreased by approximately 37.0% and 32.4%, respectively. These results demonstrate that the gradient-boosting models improve the representation of severe icing conditions relative to RF; nevertheless, the negative MBE values for all three models indicate that extreme ice thickness continues to be systematically underestimated.

The residual distributions in Figure 8 provide further evidence of the error structure across icing intensities. For low ice-thickness observations, residuals from all three models are concentrated near zero, although a slight tendency toward overestimation is observed, consistent with the positive MBE values in the low-icing subset. As the observed ice thickness increases, the residual distributions progressively shift toward negative values and become more dispersed. This pattern is particularly pronounced for RF, indicating an increasing tendency to underestimate high ice-thickness observations. XGBoost and LightGBM reduce both the magnitude and dispersion of negative residuals relative to RF, but substantial negative errors remain for some severe icing cases. The residual analysis therefore confirms that the apparently small overall bias does not imply uniform performance across the full ice-thickness range.

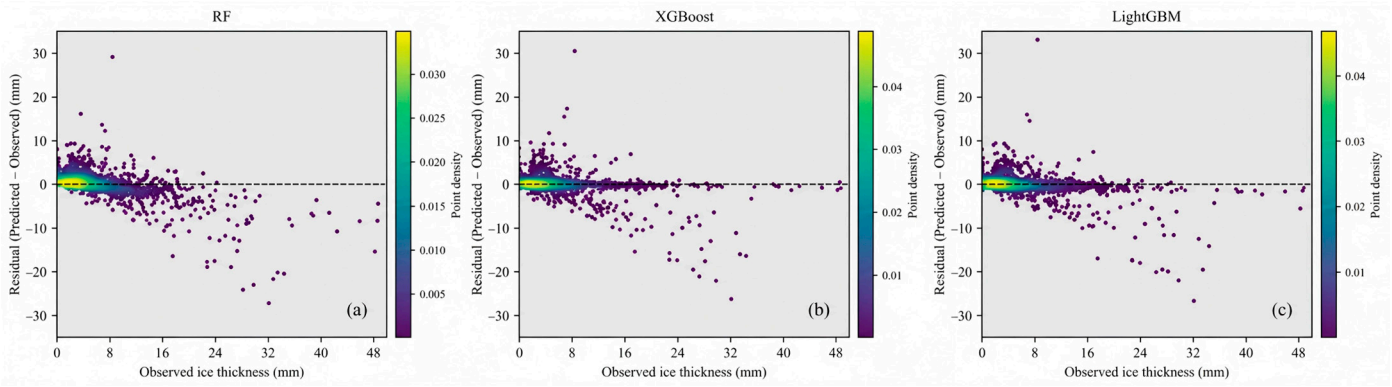


Figure 8. Residual distributions of (**a**) RF, (**b**) XGBoost, and (**c**) LightGBM as a function of observed ice thickness under station-based spatial hold-out validation. Residuals are defined as predicted minus observed ice thickness. The dashed horizontal line represents zero residual, and color indicates point density.

4.3. Feature Importance and Model Interpretation

4.3.1. Gain-Based Feature Importance of LightGBM

Figure 9 presents the gain-based feature importance ranking of the LightGBM model. Mean near-surface air temperature (tmpmean) shows the highest predictive importance, followed by longitude (lon), minimum temperature (tmpmin), maximum temperature (tmpmax), elevation, and relative humidity (rhu). This ranking indicates that temperature-related variables provide substantial information for predicting ice thickness, which is consistent with the strong thermodynamic dependence of icing processes on near-freezing atmospheric conditions. Elevation also contributes substantially to the model prediction, potentially because it represents large-scale differences in temperature, cloud/fog occurrence, and local exposure conditions in mountainous terrain. Geographic coordinates, particularly longitude, also exhibit relatively high predictive importance, suggesting that broad regional spatial gradients not fully represented by the available environmental variables are captured by the model. In contrast, NDVI, wind speed, and slope show relatively lower gain-based importance. It should be emphasized that these importance values quantify the contribution of individual predictors to the LightGBM prediction process and should not be interpreted as direct evidence of causal relationships.

4.3.2. SHAP-Based Model Interpretation

SHAP values were further used to interpret the contribution of individual features to the LightGBM predictions. For each sample, the SHAP value represents the contribution of a given feature relative to the model's baseline prediction, with the sign indicating whether the feature increases or decreases the predicted ice thickness. Figure 10a presents the global feature ranking based on the mean absolute SHAP value. Consistent with the gain-based importance results, tmpmean is the most influential predictor, followed by longitude and elevation. Latitude and the other two temperature variables (tmpmin and tmpmax) also show substantial contributions. Relative humidity, wind speed, and NDVI exhibit moderate importance, whereas aspect, slope, and precipitation contribute relatively less to the overall model output. The similarity between the two ranking approaches suggests that temperature-related variables, large-scale spatial location, and elevation constitute the main predictive information used by the model.

Figure 10b shows the SHAP beeswarm distribution, in which each point represents one observation. The horizontal position indicates the SHAP value, whereas the color represents the relative magnitude of the corresponding feature. For tmpmean, low feature values

are predominantly associated with positive SHAP values, whereas high values are mainly associated with negative SHAP values. This indicates that, within the fitted model, lower mean temperatures tend to increase the predicted ice thickness, while higher temperatures tend to suppress the prediction. Similar directional patterns are observed for tmpmin and tmpmax, although their overall contributions are smaller than that of tmpmean.

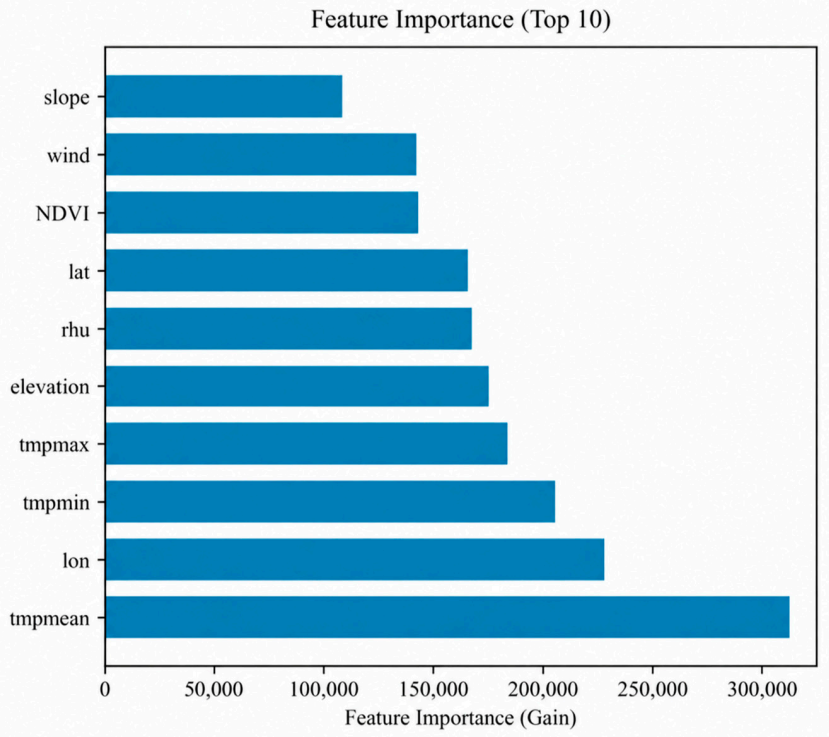


Figure 9. Top-10 feature importance ranking of the LightGBM model based on total split gain.

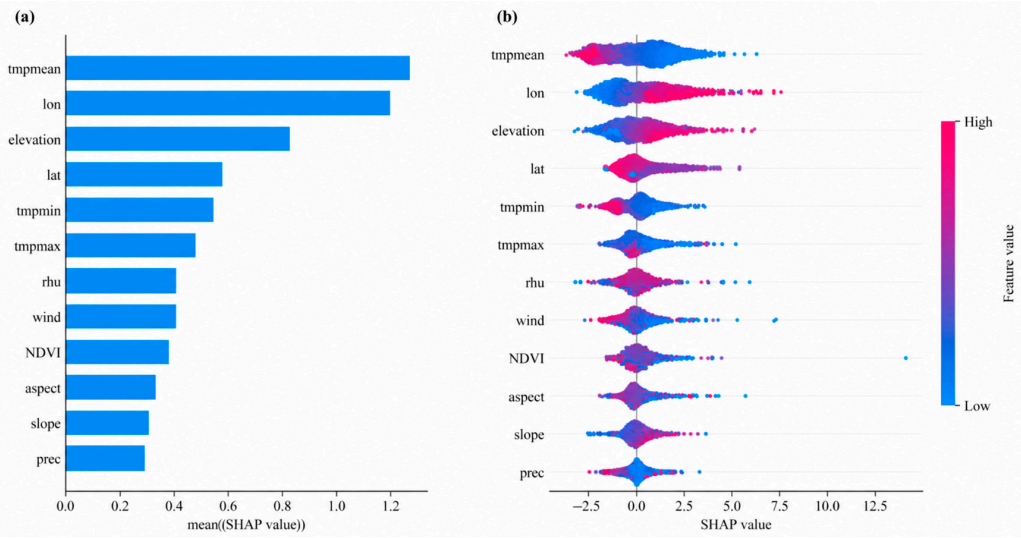


Figure 10. SHAP-based interpretation of the LightGBM model: (**a**) global feature importance quantified by mean absolute SHAP values; (**b**) SHAP beeswarm plot showing the magnitude and direction of individual feature contributions.

Elevation also shows a clear directional pattern, with higher elevations tending to be associated with positive contributions to the predicted ice thickness and lower elevations tending to contribute negatively. This model behavior is physically plausible because higher-altitude regions in Guizhou generally experience lower temperatures and more frequent

cloud/fog conditions favorable for icing. However, the SHAP results describe predictive contributions within the fitted model and should not be interpreted as direct evidence of causality. Longitude and latitude also contribute substantially to the predictions, indicating the presence of broad spatial gradients in icing conditions that are not fully represented by the available meteorological, topographic, and remote-sensing variables.

For relative humidity, wind speed, NDVI, precipitation, slope, and aspect, the SHAP distributions are more concentrated around zero and exhibit less distinct monotonic patterns. Their effects are therefore interpreted more cautiously. In particular, the SHAP summary plot alone does not provide direct evidence of interactions among predictors; therefore, no strong feature-interaction conclusion is drawn from this analysis.

It should also be noted that tmpmean, tmpmin, and tmpmax are strongly correlated, as shown in the Pearson correlation analysis. Although tree-based ensemble models are generally robust to multicollinearity in terms of predictive performance, correlated predictors may share or redistribute importance during feature attribution. Therefore, the relative ranking among the three temperature variables should not be interpreted as evidence that one specific temperature statistic is physically more fundamental than the others. Instead, their consistently high rankings collectively indicate that temperature conditions constitute one of the dominant sources of predictive information for icing thickness.

4.4. Spatial Prediction of Daily Maximum Ice Thickness

To demonstrate the regional spatial application of the trained LightGBM model, the model was applied to the 1 km gridded predictor fields over Guizhou Province for 12 January 2021. Daily meteorological variables corresponding to the same calendar date were combined with the spatially matched topographic variables, annual NDVI, longitude, and latitude at each grid cell. The resulting predictor matrix was then input into the trained LightGBM model to generate a spatially continuous estimate of daily maximum equivalent ice thickness across the study area.

Figure 11 shows pronounced spatial heterogeneity in the predicted icing field. Most grid cells are characterized by relatively low predicted ice thickness, whereas localized high-value zones occur predominantly in the western and northwestern parts of Guizhou. Across the valid prediction domain, the median predicted ice thickness is approximately 1.80 mm, while the 90th and 95th percentiles are approximately 6.66 mm and 10.05 mm, respectively. Grid cells with predicted ice thickness exceeding 10 mm account for approximately 5.1% of the valid prediction domain, while values above 15 mm are restricted to approximately 1.1% of the grid cells. The maximum gridded prediction reaches approximately 24.5 mm. These results indicate that relatively severe icing conditions are spatially concentrated rather than uniformly distributed across the province.

The western and northwestern high-value pattern is broadly consistent with the environmental characteristics represented by the model. These areas generally contain higher terrain and colder winter conditions, while the feature-importance and SHAP analyses indicate that temperature, elevation, and broad geographic gradients provide substantial predictive information for the fitted model. Therefore, the spatial pattern in Figure 11 is physically plausible within the environmental relationships learned from the monitoring data. However, this agreement should not be interpreted as evidence that elevation or any single predictor directly determines the mapped icing distribution, because the prediction reflects the combined nonlinear contributions of multiple correlated environmental variables.

The 1 km map should also be interpreted at the regional scale for which the predictor fields were harmonized. Although the finer-resolution topographic and NDVI datasets provide detailed source information, they were resampled to the common 1 km modeling grid, which inevitably smooths part of the sub-grid terrain and land-surface variability.

Consequently, localized icing differences associated with ridges, valleys, slope exposure, or other micro-terrain conditions may not be fully resolved. In addition, the mapped quantity represents the predicted daily maximum equivalent ice thickness for the selected date and should not be interpreted as a long-term extreme ice thickness, a statistically derived design ice load, or a direct replacement for site-specific transmission-line icing measurements. These limitations and the broader applicability of the spatial prediction framework are further discussed in Section 4.5.

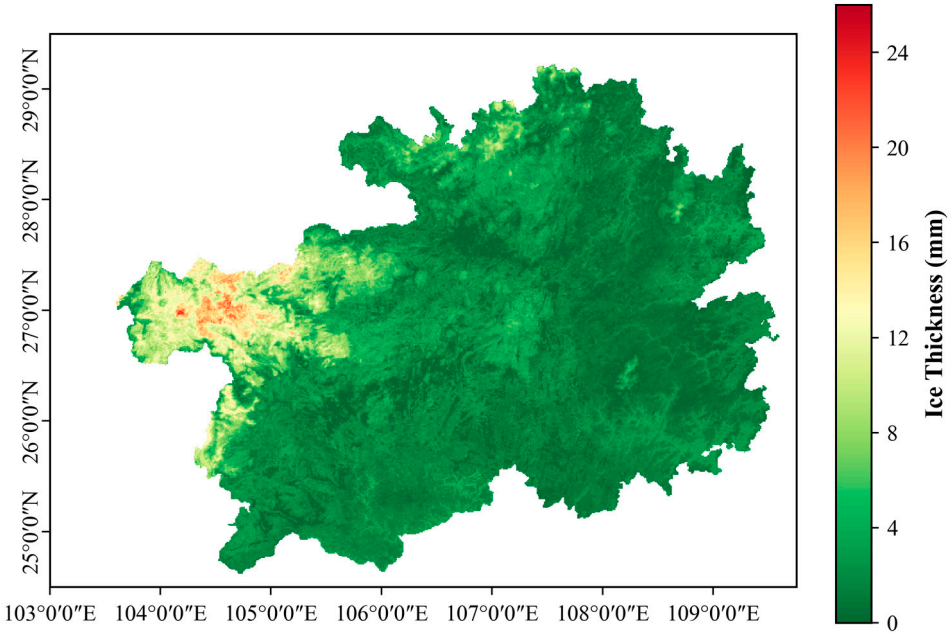


Figure 11. Spatial distribution of predicted daily maximum equivalent ice thickness over Guizhou Province at 1 km resolution on 12 January 2021.

4.5. Limitations and Applicability

The station-based spatial hold-out strategy used in this study provides a more stringent evaluation than an observation-level random split because all observations from the independent test stations were excluded from model development. Therefore, the reported performance primarily reflects spatial generalization to previously unseen monitoring locations within Guizhou Province. However, this validation does not demonstrate generalization to other climatic regions or independent time periods. In addition, although the coordinate-ablation experiment showed that the model retained substantial predictive capability after longitude and latitude were removed, the contribution of geographic coordinates indicates that some spatially structured environmental information is still not fully represented by the available predictors.

The stratified error analysis also indicates that model reliability varies with icing intensity. Although XGBoost and LightGBM performed well for the overall test set, all three models showed increasing errors and negative bias for extreme icing observations. Therefore, the proposed framework is more appropriately regarded as a regional tool for estimating the spatial distribution of daily maximum equivalent ice thickness than as a replacement for direct icing measurements or a method for determining design ice loads. Further improvement of extreme-icing prediction will require more representative severe-icing samples and additional process-related predictors.

Several data-related limitations should also be noted. To quantitatively examine the contribution of the remote-sensing vegetation descriptor, an additional sensitivity experiment was conducted by removing NDVI from the predictor set. The results of this sensitivity

analysis are presented in Table 4. The result shows that excluding NDVI changes the predictive performance from R^2 = 0.8131, RMSE = 2.5162 mm, and MAE = 1.0928 mm to R^2 = 0.7863, RMSE = 2.6905 mm, and MAE = 1.3736 mm. This comparison indicates that NDVI provides limited additional information for regional icing estimation. However, this sensitivity experiment evaluates only the contribution of NDVI as a predictor and does not quantify the complete uncertainty introduced by spatial aggregation. Because the topographic and remote-sensing datasets were harmonized to the 1 km modeling grid, sub-grid terrain heterogeneity and land-surface variability may still influence local icing conditions, particularly in complex mountainous regions.

Table 4. Sensitivity analysis of NDVI contribution.

Model Configuration	R^2	RMSE (mm)	MAE (mm)
All predictors	0.8131	2.5162	1.0928
Without NDVI	0.7863	2.6905	1.3736

In addition, several physically important micro-meteorological variables, including precipitation phase, liquid water content, droplet-size characteristics, and wind direction, were not included because they were unavailable with consistent spatial and temporal coverage in the adopted dataset. These variables may be particularly important for describing droplet impaction and freezing processes during severe icing events. Therefore, their absence represents an uncertainty source that may partly explain the increased prediction error observed for extreme icing cases.

5. Conclusions

This study developed a multi-source data fusion and machine learning framework for regional spatial prediction of daily maximum equivalent ice thickness on transmission lines in Guizhou Province. Meteorological, topographic, remote-sensing, and geographic variables were integrated with operational icing observations from 160 monitoring stations, and a station-based spatial hold-out strategy was adopted to reduce information leakage caused by repeated observations from the same locations. Under this validation framework, LightGBM achieved the highest R^2 of 0.8131 and the lowest RMSE of 2.5162 mm, while XGBoost obtained the lowest MAE of 1.0244 mm, indicating that the two gradient-boosting models showed comparable predictive performance at previously unseen monitoring locations. Stratified evaluation further showed that prediction errors increased with icing intensity, and all three models exhibited negative MBE values for observations above the 90th percentile, indicating a systematic tendency to underestimate severe icing. Gain-based feature importance and SHAP analysis showed that temperature-related variables, geographic location, and elevation provided the main predictive information for the fitted model, although these results should be interpreted as model-based attribution rather than direct physical causality because of the dependence among several predictors. The optimized LightGBM model was further applied to 1 km gridded predictor fields to generate a spatially continuous icing map for 12 January 2021, which showed clear spatial heterogeneity, with relatively high icing values mainly concentrated in western and northwestern Guizhou. Overall, the proposed framework provides a practical approach for regional estimation of daily maximum equivalent ice thickness within the study area, but it should not be regarded as a substitute for direct icing measurements or as a method for determining design ice loads. Further work should focus on improving the representation of severe icing events, incorporating additional micro-meteorological variables, and evaluating temporal and cross-regional generalization.

Author Contributions: Conceptualization, Y.W. and J.L.; methodology, Y.W., J.L. and X.N.; software, Y.W. and X.N.; validation, Y.W., B.X. and G.L.; formal analysis, Y.W.; investigation, Y.W.; data curation, Y.W.; writing—original draft preparation, Y.W.; writing—review and editing, J.L. and C.Y.; supervision, J.L.; project administration, J.L.; funding acquisition, C.Y. All authors have read and agreed to the published version of the manuscript.

Funding: This work was supported by the Science and Technology Project of China Southern Power Grid Co., Ltd., under Grant No. 060700KC23100012.

Institutional Review Board Statement: Not applicable.

Informed Consent Statement: Not applicable.

Data Availability Statement: The meteorological, topographic, and remote-sensing datasets used in this study are publicly available from the data sources described in Section 2.3. The transmission-line icing monitoring data are not publicly available due to data management restrictions of China Southern Power Grid Co., Ltd. Further information regarding the data may be obtained from the corresponding author upon reasonable request, subject to permission from the data owner.

Conflicts of Interest: Authors Yu Wu and Xianglun Nie were employed by the company Bijie Power Supply Bureau of Guizhou Power Grid Co., Ltd. The remaining authors declare that the research was conducted in the absence of any commercial or financial relationships that could be construed as a potential conflict of interest.

References

1. Li, B.; Bai, J.; He, J.; Ding, C.; Dai, X.; Ci, W.; Zhu, T.; Liao, R.; Yuan, Y. A review on superhydrophobic surface with anti-icing properties in overhead transmission lines. *Coatings* **2023**, *13*, 301. [CrossRef]
2. Sirui, Y.; Mengjie, S.; Runmiao, G.; Jiwoong, B.; Xuan, Z.; Shiqiang, Z. A review of icing prediction techniques for four typical surfaces in low-temperature natural environments. *Appl. Therm. Eng.* **2024**, *241*, 122418. [CrossRef]
3. Shen, H.; Wan, B.; Zhou, S.; Kang, J.; Chen, H.; Gao, Z. The synoptic characteristics of icing events on transmission lines in Southern China. *Atmosphere* **2023**, *14*, 1789. [CrossRef]
4. Huang, M.; Chi, C.; Gu, Y.; Zhang, Y.; Zhu, Z. Ice-shedding jump height of uneven iced sub-conductors under varying wind load conditions. *Wind Struct.* **2025**, *40*, 139–152.
5. Hou, H.; Wang, Y.; Bai, X.; Lv, J.; Cui, R.; Zhang, L.; Li, S.; Li, Z. Modelling icing growth on overhead transmission lines: Current advances and future directions. *Energy Convers. Econ.* **2024**, *5*, 343–357. [CrossRef]
6. Zhou, B.; Gu, L.; Ding, Y.; Shao, L.; Wu, Z.; Yang, X.; Li, C.; Li, Z.; Wang, X.; Cao, Y.; et al. The great 2008 Chinese ice storm: Its socioeconomic–ecological impact and sustainability lessons learned. *Bull. Am. Meteorol. Soc.* **2011**, *92*, 47–60. [CrossRef]
7. Zhang, Z.; Zhang, H.; Yue, S.; Zeng, W. A review of icing and anti-icing technology for transmission lines. *Energies* **2023**, *16*, 601. [CrossRef]
8. Ma, T.; Niu, D.; Fu, M. Icing forecasting for power transmission lines based on a wavelet support vector machine optimized by a quantum fireworks algorithm. *Appl. Sci.* **2016**, *6*, 54. [CrossRef]
9. Bai, X.; Lv, J.; Cai, D.; Shen, Y.; Wan, Y.; Hou, H. Comparative differences of physical mechanism model and data-driven model on overhead transmission line icing thickness prediction. In *Proceedings of the 2023 IEEE Sustainable Power and Energy Conference (iSPEC)*; IEEE: Piscataway, NJ, USA, 2023; pp. 1–6.
10. Molkoselkä, E.O.; Kaikkonen, V.A.; Mäkynen, A.J. Weighing Cylinder Instrument with Controlled De-Icing for Ice Accretion Measurements. In *Proceedings of the 2023 IEEE International Instrumentation and Measurement Technology Conference (I2MTC)*; IEEE: Piscataway, NJ, USA, 2023; pp. 1–6.
11. Qian, F.; Yinghua, Z.; Chunxiang, Y.; Xuefeng, L.; Xue, C.; Chenggong, G.; Xi, C.; Feng, J. Accurate Prediction of Transmission Conductor Ice Cover Thickness Based on Ice Hazard Dynamics. In *Proceedings of the 2024 5th International Conference on Power Engineering (ICPE)*; IEEE: Piscataway, NJ, USA, 2024; pp. 267–276.
12. Wang, Q.; Zhou, S.; Zhang, H.; Su, H.; Zheng, W. Prediction of conductor icing thickness based on random forest and WRF models. In *Proceedings of the 2021 International Conference on Intelligent Computing, Automation and Applications (ICAA)*; IEEE: Piscataway, NJ, USA, 2021; pp. 959–962.
13. Wang, G.; Shen, J.; Jin, M.; Huang, S.; Li, Z.; Guo, X. Prediction model for transmission line icing based on data assimilation and model integration. *Front. Environ. Sci.* **2024**, *12*, 1403426. [CrossRef]
14. Punde, P.; Birkelund, Y.; Virk, M.S.; Han, X.; Eidhammer, T. Kilometer-scale simulation of atmospheric in-cloud ground icing over complex terrain in Norwegian Arctic. *Cold Reg. Sci. Technol.* **2026**, *245*, 104851. [CrossRef]

15. Snaiki, R.; Jamali, A.; Rahem, A.; Shabani, M.; Barjenbruch, B.L. A metaheuristic-optimization-based neural network for icing prediction on transmission lines. *Cold Reg. Sci. Technol.* **2024**, *224*, 104249. [CrossRef]
16. Sim, S.; Im, J.; Park, S.; Park, H.; Ahn, M.H.; Chan, P.-W. Icing detection over East Asia from geostationary satellite data using machine learning approaches. *Remote Sens.* **2018**, *10*, 631. [CrossRef]
17. Xiong, W.; Yuan, H.; You, L. Prediction method of icing thickness of transmission line based on MEAO. *Clust. Comput.* **2018**, *21*, 845–853. [CrossRef]
18. Niu, D.; Ma, T.; Huang, Y.; Wu, M. Study on prediction of transmission line icing thickness based on ada-boost and LS-WSVM. *Int. J. Simul. Syst. Sci. Technol.* **2016**, *17*, 1. [CrossRef]
19. He, L.; Luo, J.; Zhou, X. A novel deep learning model for transmission line icing thickness prediction. In *Proceedings of the 2021 IEEE 5th Advanced Information Technology, Electronic and Automation Control Conference (IAEAC)*; IEEE: Piscataway, NJ, USA, 2021; pp. 733–738.
20. Liu, Y.; Li, Q.; Liu, J.; Li, H.; Duan, R. Research on an icing-thickness calculation model for power transmission lines based on KPCA and GWO. *Electr. Power Syst. Res.* **2025**, *248*, 111877. [CrossRef]
21. Zhou, S.; Gao, Z.; Gong, B.; Zhang, H.; Zhang, H.; He, J.; Xi, X. Ensemble Learning for Spatial Modeling of Icing Fields from Multi-Source Remote Sensing Data. *Remote Sens.* **2025**, *17*, 2155. [CrossRef]
22. Dunmire, D.; Lievens, H.; Boeykens, L.; De Lannoy, G.J. A machine learning approach for estimating snow depth across the European Alps from Sentinel-1 imagery. *Remote Sens. Environ.* **2024**, *314*, 114369. [CrossRef]
23. Maxwell, A.E.; Warner, T.A.; Fang, F. Implementation of machine-learning classification in remote sensing: An applied review. *Int. J. Remote Sens.* **2018**, *39*, 2784–2817. [CrossRef]
24. Wan, Y.; Hou, H.; Bai, X.; Lv, J.; Cai, D.; Shen, Y. Prediction of transmission line icing thickness based on long short-term memory network. In *Proceedings of the 2023 IEEE International Conference on Energy Technologies for Future Grids (ETFG)*; IEEE: Piscataway, NJ, USA, 2023; pp. 1–6.
25. Zhang, H.; Wang, S.; Shang, Z.; Zhou, Z.; Liu, Y.; Yang, Y.; Hu, X. A prediction method for overhead transmission line icing thickness based on feature attention and NGO–VMD–LSTM. *J. Renew. Sustain. Energy* **2026**, *18*, 025503. [CrossRef]
26. Roberts, D.R.; Bahn, V.; Ciuti, S.; Boyce, M.S.; Elith, J.; Guillera-Arroita, G.; Hauenstein, S.; Lahoz-Monfort, J.J.; Schröder, B.; Thuiller, W.; et al. Cross-validation strategies for data with temporal, spatial, hierarchical, or phylogenetic structure. *Ecography* **2017**, *40*, 913–929. [CrossRef]
27. Liu, T.; Zheng, Y.; Mei, L.; Lin, X.; Wang, Z.; Huang, W. Application of Mechanical Monitoring Technology for Ice Covered Overhead Distribution Conductors. In *Proceedings of the 2024 3rd International Conference on Energy and Electrical Power Systems (ICEEPS)*; IEEE: Piscataway, NJ, USA, 2024; pp. 1394–1401.
28. Bentéjac, C.; Csörgő, A.; Martínez-Muñoz, G. A comparative analysis of gradient boosting algorithms. *Artif. Intell. Rev.* **2021**, *54*, 1937–1967. [CrossRef]
29. Ke, G.; Meng, Q.; Finley, T.; Wang, T.; Chen, W.; Ma, W.; Ye, Q.; Liu, T.Y. Lightgbm: A highly efficient gradient boosting decision tree. In Proceedings of the Advances in Neural Information Processing Systems 30 (NIPS 2017), Long Beach, CA, USA, 4–9 December 2017.

Disclaimer/Publisher's Note: The statements, opinions and data contained in all publications are solely those of the individual author(s) and contributor(s) and not of MDPI and/or the editor(s). MDPI and/or the editor(s) disclaim responsibility for any injury to people or property resulting from any ideas, methods, instructions or products referred to in the content.